Journal of Colloid and Interface Science 535 (2019) 205–213

Contents lists available at ScienceDirect

Journal of Colloid and Interface Science

journal homepage: www.elsevier.com/locate/jcis

Regular Article

Understanding heat driven gelation of anionic cellulose nanofibrils: Combining saturation transfer difference (STD) NMR, small angle X-ray scattering (SAXS) and rheology ☆

Vincenzo Calabrese [a,1], Juan C. Muñoz-García [b,1], Julien Schmitt [a], Marcelo A. da Silva [a], Janet L. Scott [a,c], Jesús Angulo [b], Yaroslav Z. Khimyak [b,*], Karen J. Edler [a,*]

[a] Department of Chemistry, University of Bath, Claverton Down, Bath BA2 7AY, UK
[b] School of Pharmacy, University of East Anglia, Norwich Research Park, Norwich NR4 7TJ, UK
[c] Centre for Sustainable Chemical Technology, University of Bath, Claverton Down, Bath BA2 7AY, UK

GRAPHICAL ABSTRACT

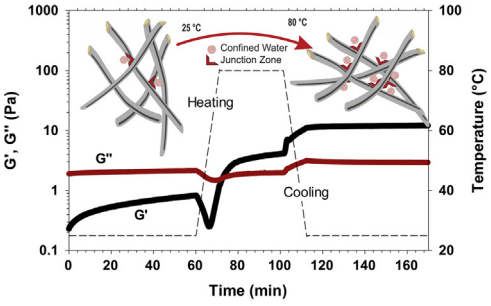

ARTICLE INFO

Article history:
Received 11 June 2018
Revised 21 September 2018
Accepted 24 September 2018
Available online 25 September 2018

Keywords:
Water confinement
Hydrogel
TEMPO oxidised cellulose
Heat induced gelation
Saturation transfer difference NMR
SAXS
Rheology

ABSTRACT

A novel mechanism of heat-triggered gelation for oxidised cellulose nanofibrils (OCNF) is reported. We demonstrate that a synergistic approach combining rheology, small-angle X-ray scattering (SAXS) and saturation transfer difference NMR (STD NMR) experiments enables a detailed characterisation of gelation at different length scales. OCNF dispersions experience an increase in solid-like behaviour upon heating as evidenced by rheological studies, associated with enhanced interfibrillar interactions measured using SAXS. Interactions result in an increased fibrillar overlap and increased population of confined water molecules monitored by STD NMR. In comparison, cationic cellulose nanofibrils (produced by reaction of cellulose with trimethylglycidylammonium chloride) were found to be heat-unresponsive.

☆ Electronic Supplementary Information (ESI) available: STD and reference NMR spectra, rheological data for other OCNF and CCNF dispersion concentrations, ^{1}H ^{13}C HSQC spectra and NOESY build up curves for OCNF before and after heating, fluorescence data, contributions to STD signal, temperature evolution of STD signal, and further NMR characterisation data. See DOI: https://doi.org//10.1039/x0xx00000x.

* Corresponding authors.
E-mail addresses: j.l.scott@bath.ac.uk (J.L. Scott), j.angulo@uea.ac.uk (J. Angulo), y.khimyak@uea.ac.uk (Y.Z. Khimyak), k.edler@bath.ac.uk (K.J. Edler).
[1] The authors contributed equally to the work.

https://doi.org/10.1016/j.jcis.2018.09.085
0021-9797/

1. Introduction

There is an enormous interest in cellulose based hydrogels as inexpensive and biodegradable gels, for their industrial and sustainable applications. Cellulose naturally occurs in plant cell walls as a hierarchical assembly of fibrils, tightly bonded via multiple hydrogen bonds [1,2]. Cellulose and cellulose derivatives are becoming of great importance for the production of a wide range of biodegradable materials, as their rheological properties have gained great importance for several applications ranging from drug release [3], microbeads [4], to functional ingredients in food (e.g. thickeners, stabilizers, gelling agents) [5–7].

Due to strong attractive forces between fibrils, cellulose aqueous dispersions have poor stability, which can be improved by the introduction of repulsive interactions [8]. For instance, the 2,2,6,6-tetramethylpiperidine-1-oxyl radical (TEMPO)-mediated oxidation of the primary OH groups is one of the most commonly used surface modifications, which selectively introduces negatively charged carboxylate groups at the C6 position of the glucose rings of cellulose [9–11]. The TEMPO-mediated oxidation yields stable anionic oxidised cellulose nanofibrils (OCNF) with high surface charge (ζ-potential < −30 mV) [12]. The large aspect ratio of OCNF (5 nm diameter, up to few μm length) leads to a low overlap concentration (i.e., the minimum volume fraction of particle necessary for particle-particle interactions to occur) and hydrogels can form with a water content up to 99.9% [8,13,14]. The gelation properties of OCNF aqueous dispersions have been widely investigated under different conditions by varying pH [8], electrolyte [12,15] and surfactant [6,14] concentrations, showing a wide span of rheological properties. In several studies, cation-induced gelation of OCNF, due to screening of the negative charges, has been reported [12,15,16]. Crawford et al. first demonstrated a surfactant-induced gelation, proposing either a depletion flocculation mechanism or a micellar crosslinking between fibrils [6]. More recently, stable shear thinning dispersions have been also reported using cationic cellulose nanofibrils (CCNF) [17,18]. However, to the best of our knowledge, the gelation of OCNF dispersions triggered only by temperature has never been reported before. Previous gelation processes have required addition of acids, oppositely charged ions or surfactants.

In this work, we investigate a yet unreported reversible physical gelation induced by temperature alone without any structural or chemical change in the OCNF. By raising the temperature, weak physicals gels were obtained from OCNF dispersions. Further rheological investigations revealed the reversibility of the process. Since the only input to this system was the increased temperature, we hypothesised that the interactions between the OCNF and water could be important to understand the mechanism of gelation. Studies of the structure and dynamics of water by NMR have so far largely relied on the determination of ^{1}H T_1 and T_2 relaxation times [19,20]. However, while the former can be misinterpreted due to its symmetric behaviour at short and long correlation times (i.e. high T_1 times might indicate either very fast or very slow dynamics), the latter is strongly affected by the kinetics of chemical exchange, thus hindering the real impact of molecular motion on T_2 relaxation. On these grounds, we have instead used an NMR approach based on the saturation transfer difference (STD) experiment on D_2O hydrogel samples which overcomes the drawbacks of NMR relaxation measurements. It is based on monitoring the STD signal of the residually protonated water (HDO) in hydrogel samples prepared in D_2O. It should be noted that STD NMR has been applied before to the study of small molecule gelators focusing on the NMR signals of the gelator, but the technique is restricted to relatively small molecules even using high field NMR [21]. Here, we demonstrate that STD NMR can be used to easily follow the changes in water confinement in systems constituted by nanoparticulate gelators (cellulose derivatives) undergoing a sol-to-gel transition. Hence, herein we describe the reversible heat-induced gelation of OCNF aqueous dispersion. Coupling STD-NMR with rheology measurements and small angle x-ray scattering to determine network structures, provides detailed structural insights into the gelation mechanisms upon increased temperature, both at the mesoscale level and at the molecular level.

2. Materials and methods

2.1. Sample preparation

OCNF, prepared as described previously using a TEMPO/NaOCl/NaBr oxidation [13] followed by high pressure homogenization, were provided by Croda, as a solid paste in water (ca. 8 wt% OCNF). The degree of oxidation was determined to be 25% (ζ-potential ∼ −55 mV), measured by conductometric titration [13,22,23].

CCNF with a degree of substitution of 26% (ζ-potential ∼ +50 mV) were obtained treating α-cellulose (product number C8002) powder with glycidyltrimethylammonium chloride (≥90%) (GTMAC), both purchased from Sigma-Aldrich®. Ethanol (>95%), NaOH (≥97%) and HCl (37%) were purchased from Sigma-Aldrich®. Ultrapure deionized water, DI, (18.2 MΩ·cm) was used throughout.

OCNF were purified by dialysis to remove residual salts and preservatives [24]. Approximatively 20 g of OCNF were suspended in 100 mL of DI and stirred at room temperature for 30 min, the dispersion acidified to pH 3 using 1 M HCl (aq) and dialysed against DI (Sigma-Aldrich® cellulose dialysis tubing, molecular weight cut-off of 12,400 Da) for 3 days with daily replacement of DI. The dialysed OCNF were processed via mechanical shear (ULTRA TURRAX, IKA T25 digital, 30 min at 6500 rpm) and the pH adjusted to 7 using 0.1 M NaOH (aq). After a second dialysis step (as previously reported) the dispersion was diluted to *ca* 2 wt% (dry basis) and dispersed by sonication: Ultrasonic Processor FB-505, Fisher, 200 W·cm^{-2}, equipped with a 1 cm probe, using a series of 1 s on 1 s off in pulse mode for a net time of 5 mins at 60% amplitude on *ca* 45 mL dispersion contained in an ice bath. The GTMAC grafting of α-cellulose was carried out following the semi-dry protocol suggested by Zaman et al. [18]. The functionalization was performed using 1 g of NaOH, 20 g of α-cellulose, 7.2 g of DI and 36.4 g of GTMAC. The CCNF dispersion was dialysed and dispersed as previously described for OCNF. The solid contents (wt%) of the OCNF and CCNF dispersions were obtained by drying approximately 10 g of the dispersion in an oven at 60 °C until constant mass was achieved. The final concentration was calculated based on the average of three measurements. Specific concentrations of OCNF and CCNF dispersions were obtained via dilution of the stock dispersions.

2.2. Rheology

The rheological measurements were performed using a stress-controlled rheometer (Discovery HR3, TA instruments®) equipped with a sandblasted plate-plate geometry (40 mm). The samples were used without any further processing and the edge of the sample was covered with a thin layer of mineral oil to prevent evaporation and further covered with a solvent trap to ensure homogeneity of temperature within the chamber. Two types of experiments were conducted. Small amplitude oscillatory shear (SAOS) experiments at 0.1% strain and 10 rad s^{-1} angular frequency and steady state flow curves. The SAOS rheology experi-

ments were performed within the linear viscoelastic region as determined by amplitude and frequency sweeps experiments. To establish the same deformational history for all the samples, 1 min of rotational pre-shear at constant shear of 1 s^{-1} was applied, afterwards, the samples were subject to the following sequence of experiments: (*i*) thixotropy loop with increase in shear rate from 0.1 to 100 s^{-1} in 161 s, then reversed; (*ii*) SAOS-time ramp of 60 min; (*iii*) SAOS-heating ramp, from 25 to 80 °C with a heating rate of 5 °C min^{-1}; (*iv*) SAOS-time ramp of 30 min; (*v*) SAOS-cooling ramp, from 80 to 25 °C with a heating rate of 5 °C min^{-1}; (*vi*) SAOS-time ramp of 60 min and (*vii*) thixotropy loop as described in (*i*).

The percentage recoverable energy, *RE%*, derived from the thixotropy loop was obtained by Eq. (1), where A_i is the area under the shear viscosity curve upon increase of shear rate (0.1–100 s^{-1}) and A_d is the area under the shear viscosity curve upon decrease of shear rate (100–0.1 s^{-1}).

$$RE\% = \left(\frac{A_d}{A_i}\right)100 \quad (1)$$

In addition, a power law model [25], Eq. (2), for the shear viscosity from 0.1 to 100 s^{-1} was used to describe the magnitude of the shear-thinning behaviour.

$$\eta \propto \dot{\gamma}^n \quad (2)$$

where $\dot{\gamma}$ is the shear rate and n is the power law exponent, which can be derived from the slope of the curve in the logarithmic representation.

2.3. Fluorescent probe

Surface hydrophobicity of OCNF was probed using the fluorescent probe 6-propionyl-2-(*N*,*N*-dimethylamino)- naphthalene (PRODAN, ≥98.0% Sigma-Aldrich®). A PRODAN in methanol (≥98.0% Sigma-Aldrich®) stock solution of 0.32% [w/v] was prepared and stored in the dark at 15 °C. 10 μL of the PRODAN stock solution was added to 2 mL OCNF dispersions at 0.012, 0.05 and 0.1 wt% before and after heating (80 °C for 30 min) followed by gentle shaking. The measurements were performed in the dark after the samples were kept in the dark for at least 2 h prior to measurement. The relative fluorescence intensity (RFI) was measured in a spectrofluorometer (Perkin Elmer LS 50B) as a function of the emission scan. The excitation wavelength used was 365 nm and the emission scanned from 400 to 650 nm with excitation slit widths at 5 nm as reported by Haskard et al. [26].

2.4. UV-visible spectrophotometry

Measurement of transmitted light (%) was used to detect interfibrillar aggregation using a UV-Vis spectrophotometer (Agilent®/HP 8453). Dispersions were degassed (in a sonicating bath), and loaded into a quartz cuvette (Hellma Analytics®, 1 × 1 × 5 cm). Subsequently, a layer of mineral oil was placed on the top of the dispersions to prevent solvent evaporation during the heating process. The cuvette was immersed for 2/3 of its height in a water bath at 80 °C for 30 min, ensuring that the dispersion was completely immersed below the water-bath level. The samples were equilibrated at room temperature for at least 2 h before measurements. The transmittance spectrum was obtained between 500 and 800 nm and plotted as function of wavelength (nm).

2.5. Small angle X-ray scattering (SAXS)

Small angle X-ray scattering (SAXS) measurements were performed at Diamond light source (Didcot, Oxfordshire), on the I22 beamline with a beam energy E = 12.4 keV and wavelength λ = 1 Å. The data were collected using a Pilatus P3-2M (Silicon hybrid pixel detector, DECTRIS) with a total acquisition time of 7 s (as an average of multiple frames of 100 ms). The probed q-range was 0.005–0.75 $Å^{-1}$ where q is the scattering vector. The samples were loaded into glass capillary tubes (Capillary tube supplies Ltd®) of 1.5 mm external diameter. To avoid solvent evaporation, heated samples were sealed with mineral oil and prepared in a water bath at 80 °C for 30 min followed by cooling at room temperature. The measured scattered intensity $I(q)$ (cm^{-1}) is defined for dilute isotropic suspensions as follows [27]

$$I(q) = \varphi V_p(\Delta p)^2 P(q) S(q) + bkg \quad (3)$$

where φ is the volume fraction occupied by the particles, V_p is the volume of the particles (in cm^3), Δp is the difference in scattering length density between the dispersed particles and the solvent (in cm^{-2}), $P(q)$ is the normalized form factor which describes the shape and size of the particles, $S(q)$ is the structure factor and describes interference of the X-ray beam with multiple objects, usually associated with particle-particle interactions, and *bkg* is the background. The scattering data were background subtracted, and, in agreement with the particle morphology observed in transmission electron microscopy (TEM) measurements [13,18], cellulose fibrils were modelled as rigid cylinders with an elliptical cross section and a uniform scattering length density. As such, the major radius of the cross-section (r_a) and radius axial ratio (ρ) were fitted variables while the value of the fibril length (L) was kept fixed in agreement with previous TEM measurements, 300 and 1000 nm respectively for CCNF [18,28] and OCNF [13]. The interactions between the rigid fibrils were modelled using the Random Phase Approximation (RPA) [27,29,30], with the parameter ν_{RPA} describing the strength of the interactions. Positive values of ν_{RPA} are associated with repulsive interaction between rods, while negative values are associated with attractive interactions. This model, based on mean-field theory has been studied extensively in the literature and recently applied for oxidised cellulose nanofibrils [31].

2.6. Nuclear magnetic resonance spectroscopy

All the solution state NMR experiments were carried out using a Bruker Avance I spectrometer operating at a ^1H frequency of 499.69 MHz equipped with a 5 mm probe. Around 700 μL of dispersion (4 and 1 wt%) in 99.9% D_2O (Sigma-Aldrich®) was pipetted into a 5 mm NMR tube at room temperature. It should be noted that the cellulose dispersions (OCNF and CCNF) were not solvent exchanged in D_2O beforehand; therefore, the final concentration of exchangeable protons (hence HDO) in the gels was proportional to the OCNF and CCNF concentrations used (1 and 4 wt%). Variable temperature (VT) experiments were performed from 25 to 80 °C, at different intervals, allowing thermal stabilisation of the sample for 20 min before acquisition. All the experiments were carried out using a 5 s relaxation delay. The analysis of the NMR spectra was focused on the HDO residual signal.

^1H–^{13}C HSQC and NOESY experiments were carried out for the characterisation of OCNF 1 wt%, before and after heating the sample at 80 °C (^1H spectrum of CCNF 1 wt% showed very large broadening precluding further characterisation). A coaxial tube containing toluene-d_8 was used within the 5 mm NMR tube for chemical shift referencing at different temperatures. Thus, ^1H and ^1H–^{13}C HSQC experiments were referenced to the chemical shift values of the residual methyl peak of toluene-d_8 (2.08 ppm) [5]. Phase-sensitive HSQC experiments with ^1H–^{13}C correlation via double inept transfer were acquired with 256 increments in the F1 dimension. Phase-sensitive NOESY experiments with water

suppression with gradients were carried out at 100, 200, 300, 400 and 500 ms mixing time with 128 increments in F1.

Saturation Transfer Difference (STD) NMR experiments [32] were performed by selective ^{1}H saturation of the OCNF and CCNF networks (resonances below 0 ppm), employing a spoil sequence to remove unwanted magnetization. Cascades of 49 ms Gaussian-shaped pulses at a field strength of 50 Hz were employed, with a delay of 4 μs between successive pulses, for a total saturation time of 4 s. The *on*-resonance and *off*-resonance frequencies were set to −1 and 50 ppm, respectively, and a recycle delay of 5 s was used. The STD spectra were obtained by subtracting the *on*- from the *off*-resonance spectrum (I_{sat} and I_0, respectively, †ESI, Figs. S1 and S2). To determine the STD response (η_{STD}) of the HDO peak (which is proportional to the fraction of bound HDO), its signal intensity in the difference spectrum (I_{STD}) was integrated relative to the signal intensity in the *off*-resonance spectrum (I_0) [33].

$$\eta_{STD} = \left(\frac{I_0 - I_{sat}}{I_0}\right)100 = \left(\frac{I_{STD}}{I_0}\right)100 \quad (4)$$

3. Results and discussion

Examination of the rheological behaviour of CCNF dispersions showed no effect of temperature. However, OCNF dispersions revealed a striking sol-to-gel transition upon heating, never observed before, to our knowledge, for a cellulose-based dispersion (Fig. 1).

3.1. Evidencing the heat-induced gelation of OCNF dispersions: rheology

The 1.25 wt% OCNF dispersion sol-to-gel transition was analysed using measurements of storage (G′) and loss (G″) moduli of the dispersion as a function of temperature and compared with a 1 wt% CCNF dispersion (Fig. 1, †ESI, Fig. S3 for OCNF at 1, 1.5, 1.75 and 4 wt%). In the first time ramp, the OCNF dispersion showed a time dependent G′ similar to the behaviour observed by Veen et al. [34] for bacterial cellulose dispersions, associated with the reformation of the cellulose fibrillar contacts after disruption of the network induced by the loading of the sample in the rheometer. During the temperature ramp, G′ sharply increased with temperature rise from 25 to 80 °C, then reached equilibration at 80 °C. Surprisingly, G′ continued to increase upon cooling (from 80 to 25 °C). The evolution of G′ and G″ upon heating, with G′<G″ before heating and G′ > G″ after heating, indicates that the OCNF dispersion underwent a heat-induced sol-to-gel transition. It is noted that the OCNF dispersion showed an increase in G′ of one order of magnitude upon heating, while the value of G" remains constant. As such, the system increased in overall elasticity (G′), while the viscous component (G″) remained constant. After cooling down to room temperature, G′ and G″ remained constant. For CCNF dispersions a slight increase in G′ was observed upon equilibration at 80 °C, but neither G′ nor G" changed significantly upon heating, indicating that, unlike OCNF, the rheological properties of the CCNF dispersions are insensitive to the heating process at this concentration.

In order to gain information regarding the rearrangement of the network upon shear of the non-heated OCNF and heated OCNF (OCNF*), we carried out thixotropy loop experiments, before and after the heating loop previously described (*in situ* heating). It is noted that the results of the thixotropy loop are strictly dependent on the time frame in which the increase and decrease of the shear rate occurs. Due to this, a faster thixotropic loop could produce a different outcome than a slower loop. Regardless, as the conditions

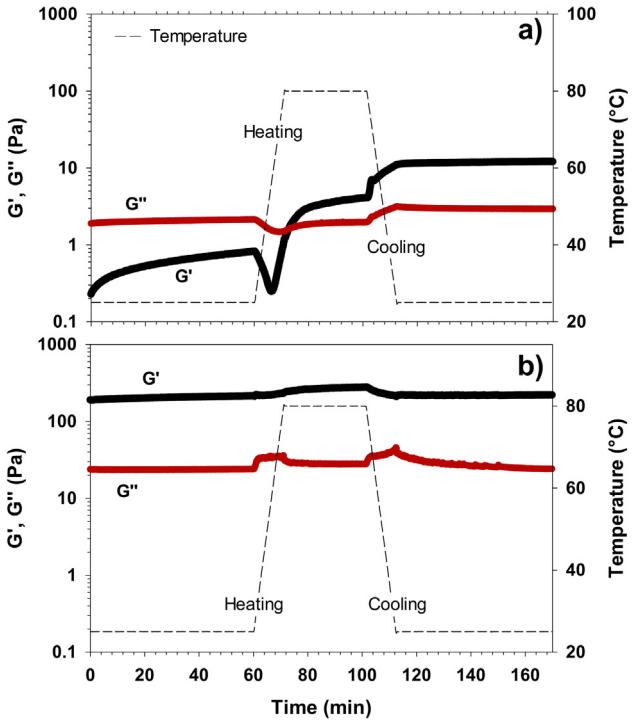

Fig. 1. Storage (G′) and loss (G″) moduli as function of temperature and time, (a) 1.25 wt% OCNF dispersion and (b) 1 wt% CCNF dispersion. The OCNF solid content of 1.25 wt% was selected over 1 wt% as the heat-induced gelation effect is more pronounced at this concentration (†ESI, Fig. S3 for OCNF at 1, 1.5 and 1.75 wt%). (ii) The concentration of the fibrils used in all experiments is well above the overlap concentration, calculated to be substantially less than 0.1 wt% [6]. Error for intrinsic limitation of sample loading and equipment of ca. 5%. This is within the size of the symbols used on the graphs.

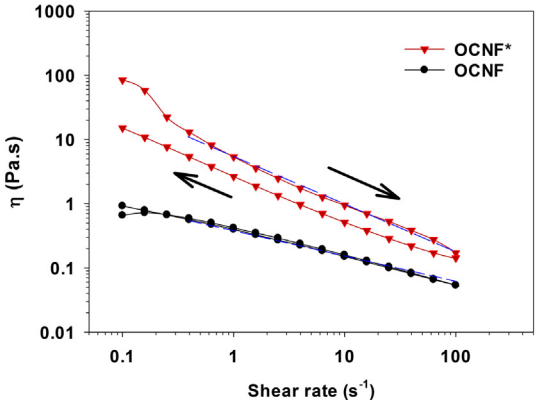

Fig. 2. Shear viscosity loop (Pa·s) of OCNF and OCNF* (heated) 1.25 wt% dispersions. The increase and decrease of the shear (s^{-1}) is indicated by the arrows. The dashed line corresponds to the fitted power law model (Eq. (2), for shear rate from 0.39 to 100 s^{-1}, $R^2 > 0.99$). Error for intrinsic limitation of sample loading and equipment of ca. 5%. This is within the size of the symbols used on the graphs.

for each loop remain the same, the thixotropy loop provides comparable information about the material.

At first the shear viscosity of the OCNF* dispersion had a value almost two orders of magnitude greater than that of the OCNF dispersion (at 0.1 s^{-1}), confirming that the OCNF forms a stronger network upon heating (Fig. 2). The OCNF dispersion is a non-thixotropic fluid, indicating that particle interactions are quickly restored after disruption induced by shear flow [35]. On the contrary, the OCNF* dispersion showed a considerable work softening behaviour [36] characteristic of gel-like materials, where a slow

regeneration of the colloidal aggregates occurs [25]. Similar trends have been observed for cellulose nanocrystals [35], CCNF [17] and bacterial cellulose [37] dispersions at concentrations beyond the gelation threshold [17,35,37] but never a heat-induced change in thixotropy as for the 1.25 wt% OCNF dispersion. In addition, the non-thixotropic OCNF and the work softening OCNF* dispersions were underlined by a significant difference in recoverable energy, *RE%*, 97% and 51% respectively (Eq. (1)). The intensity of the shear-thinning behaviour described by the exponent *n* of a power law model (Eq. (2)) resulted in greater values for OCNF* compared to OCNF, 0.74 and 0.15 respectively, indicating the presence of a stronger network, which decays more significantly upon shearing [24].

Further rheological measurements performed on OCNF* dispersions showed a complete loss of gel-like properties when the heating loop was made prior to the loading of the sample into the rheometer. In this situation, the OCNF* dispersion showed similar rheological properties compared to the OCNF dispersions, indicating that the perturbation occurring during loading is enough to induce a complete gel-to-sol transition. Nevertheless, the thixotropy loop of the *in situ* prepared OCNF* dispersion showed only partial breakage of the network, with incomplete restoration of the viscosity observed prior to heating. Thus, the difference in rheological properties between the water bath and the *in situ* heated OCNF dispersions indicates that a complete gel-to-sol transition is obtained either at higher shear rates (>100 s^{-1}), or upon other forms of perturbation (*e.g.* shaking) prior to measurements.

To better understand the heat induced gelation mechanism of OCNF dispersions, we combined SAXS and UV-Vis measurements to investigate the aggregation state of fibrils at the mesoscale level, and NMR spectroscopy to probe molecular scale changes of water confinement in the OCNF hydrogel.

3.2. Structural information at the mesoscale level: UV-Vis and SAXS

The strong influence of the deformational history on the gel properties of OCNF dispersions, as observed in the thixotropy loops (Fig. 2), required non-invasive, *in situ*, techniques to better understand the sol-to-gel transition. To that aim, SAXS and UV-Vis experiments were carried out to track the impact of temperature on the aggregation state of the fibrils at the mesoscale level. In particular, SAXS experiments allow a quantitative description of the aggregation state of the fibrils.

The UV-Vis spectra clearly showed a lower transmittance for the 1 wt% OCNF* compared to the OCNF, indicating that the aggregation of the OCNF fibrils is enhanced upon heating (Fig. 3) [15].

The microstructure of the 1 wt% OCNF and CCNF dispersion were probed using SAXS (Fig. 4). In all the SAXS curves, the Guinier region was not observed in the low *q*-range, showing that the overall fibril length is greater than the length scale probed in this experiment (> 125 nm) [38]. Nevertheless, the SAXS patterns showed two clear regions for the OCNF dispersions: a high *q*-range for $q > 0.1$ Å^{-1} associated with the fibril cross-section and a low *q*-range for $q < 0.1$ Å^{-1} linked to the elongated aspect of the fibrils. In the high *q*-range, the intensities $I(q)$ of OCNF and OCNF* were superimposable in absolute scaling, indicating that the cross-section of the fibrils is not influenced by the heating process. On the contrary, in the low *q*-range, a significant difference in signal intensity was observed between the OCNF and OCNF* dispersions. In the low *q*-range the signal intensity of the OCNF dispersion followed a q^{-1} slope (dashed line on Fig. 4a) which is characteristic of rigid rods [38] and in agreement with the SAXS [39] and small angle neutron scattering (SANS) [40,41] data previously reported. After heating, the intensity increased and followed a $q^{-1.67}$ slope. In agreement with rheological data, the CCNF did not show strong variations between the non-heated CCNF and the heated CCNF (CCNF*), the two curves being almost completely superimposable. It can be noted concerning the slope in the low *q*-range, that the patterns deviate from the q^{-1} slope, indicating that the fibrils are already aggregated before heating, in agreement with the gel state observed for CCNF in rheology before heating.

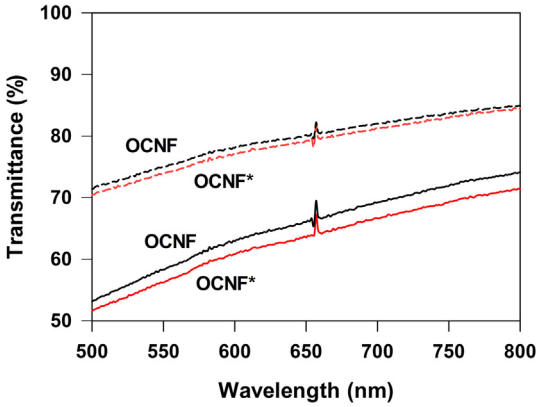

Fig. 3. UV-Vis transmittance spectra of the OCNF and OCNF* dispersions at 0.5 and 1 wt%, dashed and solid line respectively. Error for intrinsic limitation of the equipment of ca. 1% is within the width of the line.

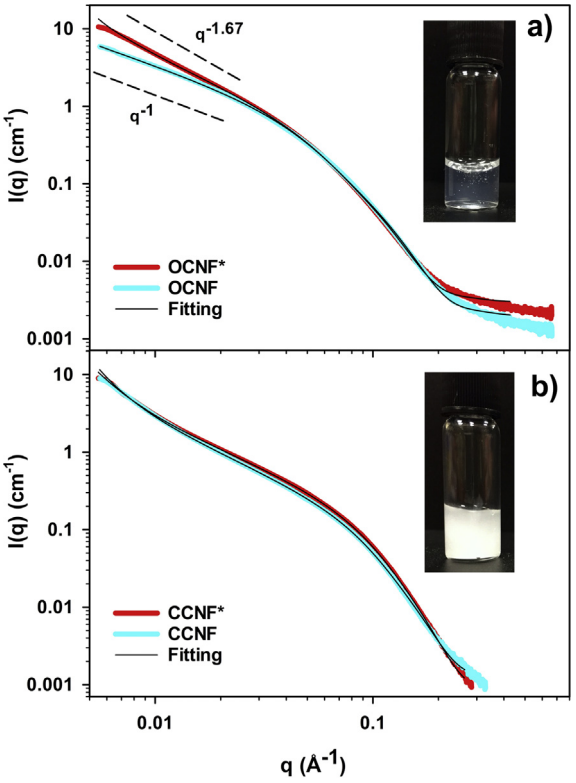

Fig. 4. SAXS patterns for (a) 1 wt% OCNF (in blue) and OCNF* (in red) dispersions and (b) 1 wt% CCNF (in blue) and CCNF* (in red) dispersions. Intensity is given in absolute scaling (cm^{-1}), errors in the value of the intensity are given on the graph. The black lines are the fits given by a model of interacting rigid cylinders with an elliptical cross-section. Dashed lines indicate the slopes where D_m is obtained. For CCNF and CCNF*, the slope in the *q*-range 0.02–0.06 Å^{-1} is $\sim q^{-1}$ as expected for fibrillar objects. Images of 1 wt% OCNF and CCNF dispersions are shown as insets.

The best data fitting for both OCNF and CCNF was obtained using a model of interacting rigid cylinders, with interactions modelled using the Random Phase Approximation (Table 1) [27,29,30]. The parameter v_{RPA} describes, from the aggregation state of the cellulose fibrils, information regarding the interfibrillar interactions.

Table 1
Values of the fitted SAXS data for 1 wt% OCNF, OCNF*, CCNF and CCNF* dispersions.

	Length (nm)[a]	Major radius (nm)[b]	Radius axial ratio	ν_{RPA}[c]	D_m
OCNF	1000	4.3 ± 0.1	0.30 ± 0.03	0	1.00
OCNF*	1000	4.3 ± 0.1	0.31 ± 0.03	−19.8 ± 0.5	1.67
CCNF	300	2.6 ± 0.1	0.46 ± 0.03	−5.1 ± 0.5	\
CCNF*	300	2.7 ± 0.1	0.45 ± 0.03	−7.4 ± 0.5	\

[a] The length of the fibrils was kept fixed at the values given by the literature for the CCNF [18,28] and OCNF [13].
[b] The polydispersity over the cross-section was found to be 20%.
[c] For OCNF, interactions were not needed to fit the data, hence ν_{RPA} was fixed at 0.

For OCNF, ν_{RPA} was null due to non-interacting behaviour of the fibrils. On the contrary, the ν_{RPA} parameter was found to be −19.8 for OCNF*, suggesting interfibrillar attractive interactions as indicated by the negative value of ν_{RPA}. For CCNF, the signal can be modelled well by interacting rigid fibrils before and after heating, in both cases with the addition of a q^{-4} signal at very low q-range to describe the presence of larger aggregates as suggested by a more turbid dispersion (Fig. 4b inset) and gel-like behaviour. In that case as well, heating seemed to further decrease the ν_{RPA} value, although the change is less pronounced and in the low-q region the two curves superimposed. The strong interactions between CCNF explains, therefore, the minimal CCNF rearrangement upon heating.

It is noted that, in the model of fibril-fibril interaction employed herein, the actual value of ν_{RPA} will be dependent on the length of the nanofibrils (fixed at 300 and 1000 nm for CCNF and OCNF respectively). Nonetheless, assuming the fibril form-factor is unchanged with changes in temperature, the trends observed in the variation of ν_{RPA} upon heating are valid. The SAXS results suggest that non-attractive OCNF experience a change in fibril-fibril interaction upon heating, leading to gelation. A similar phenomenon was previously observed upon addition of salt, where reduction of the electrostatic repulsion between OCNF led to gelation [31].

The aggregation of OCNF was also evaluated in terms of fractal theory. The mass fractal dimension (D_m), obtained from the slope in the low-q power law region, showed a noteworthy increase in D_m upon heating, indicating the formation of a more space spanning network [41,42]. In a recent study, Wu et al. [43] showed the primary importance of the particle shape over the material properties and that the assembly of elongated particles diverge significantly from the reaction-limited cluster aggregation (RLCA) and diffusion-limited cluster aggregation (DLCA) previously proposed for spherical colloidal particles [44]. Interestingly, Wu et al. [43] reported values of D_m for asbestos and glass rod-like particles nearly equal to the D_m values of OCNF* shown here (Table 1).

3.3. Monitoring changes in water confinement during gelation: NMR relaxation and saturation transfer difference (STD NMR) of residually protonated water (HDO)

While UV-Vis and SAXS yielded a mesoscopic picture of OCNF heat-induced gelation, providing information about changes in fibril-fibril interactions, solution NMR spectroscopy could be used to probe the gelation at the molecular level in terms of water dynamics. It is well known that NMR not only provides information on the chemical nature and conformation of molecules but also allows the investigation of the dynamics of the individual components (molecular motions) [45,46]. Importantly, solution-state NMR has already been employed to provide direct surface characterisation of nanocellulose and TEMPO-oxidised nanocellulose in aqueous colloidal suspensions [47]. Only the nuclei at the surface of cellulose fibres are visible by solution NMR, as those in the core are not detected due to their very short T_2 relaxation time (large signal broadening).

In this work, we have focused on the analysis of the residually protonated water peak (HDO) in the dispersions prepared in D_2O, which originates from the ^1H-$^2H(D)$ exchange due to fibril-D_2O interactions. In this regard, it is important to note that O'Neill et al. recently demonstrated by deuterium labelling, neutron scattering and molecular dynamics simulations that there exist two well differentiated populations of water associated with cellulose [48]. One is more mobile and can be associated with surface water, and the second population is consistent with confined water that can be attributed to water present in the narrow spaces between fibrils. Importantly, ^1H-^{13}C HSQC and NOESY experiments carried out before and after heating of the OCNF gels at 80 °C showed no change in the chemical environment or conformation, respectively, at the surface of OCNF fibrils upon heat-induced gelation (†ESI, Figs. S4 and S5), in agreement with fluorescent spectroscopy which confirmed the unchanged hydrophobicity of the fibrils after heating (†ESI, Fig. S6). As neither the dimensions of OCNF nanofibrils, nor the conformation of the surface moieties changed upon heating, as shown by SAXS (Fig. 4, Table 1) and NMR (†ESI, Figs. S4 and S5) respectively, we can reasonably assume that the fraction of surface water is not affected significantly by heating. On these grounds, we have focused our NMR discussion on the role of water in terms of changes in the fraction of confined water, as presented below.

Due to the intrinsic limitations of T_1 and T_2 relaxation measurements, we developed a new methodology based on Saturation Transfer Difference NMR (STD NMR) spectroscopy [49] to monitor the behaviour of water in the gels upon heating and to correlate with our rheological observations. STD NMR is a very well-known ligand-based NMR technique for the characterisation of binding of small molecules to macromolecular receptors, and it has already been applied to study the exchange phenomena of small organo- and hydrogelators between the free state, in the isotropic phase of the gel, and the bound state, in the anisotropic network [21,50]. To the best of our knowledge, it has never been employed to study the evolution of the state of water during the gelation process. Here, we focus on monitoring the residually protonated water molecules (HDO) during the process of gelation. Briefly, by irradiating ^1H resonances corresponding to the core of the cellulose network (1 ppm), we can observe the binding of water to the surface of cellulose fibrils. Importantly, the measured STD factor is directly proportional to the fraction of OCNF-confined water (f_{BW}) when the experiments are carried out in D_2O gels. Under these conditions we can safely discard any significant contribution from direct saturation transfer through chemical exchange of HDO with the hydroxyl groups of cellulose, as the majority of them will be deuterated, compared to the enormous network of non-exchangeable sugar protons available to transfer magnetization to bound HDO molecules by inter-molecular NOE (schematic representation †ESI, Fig. S7).

On these grounds, we measured the STD factors of the residual HDO water peak for OCNF and CCNF gels prepared in D_2O at different temperatures (Fig. 5, for non-normalised data †ESI, Fig. S8). Notably, the results showed a striking difference between OCNF and CCNF dispersions. While in OCNF dispersion the STD factors

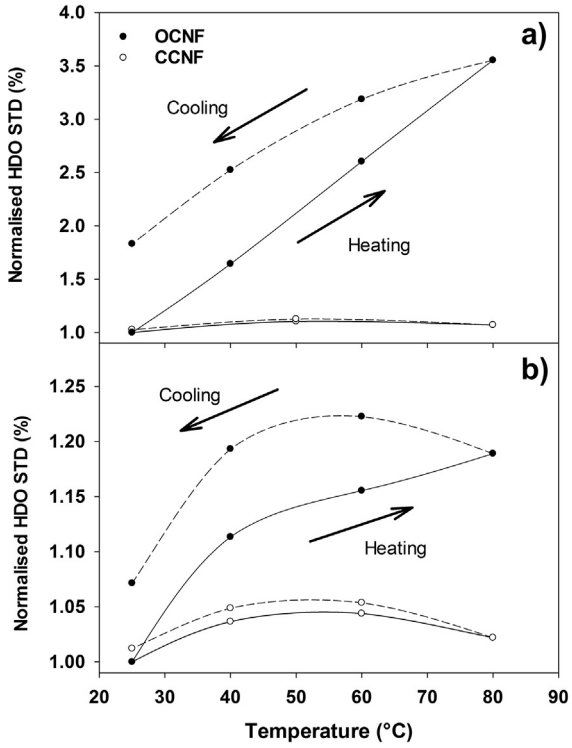

Fig. 5. Temperature evolution of the ^{1}H HDO STD factor for OCNF (solid circles) and CCNF (empty circles) dispersions (a) 1 wt% and (b) 4 wt%, during heating (solid line) and cooling (dashed line) cycles. An *on-resonance* frequency of −1 ppm was used to saturate the OCNF and CCNF networks. The STD values are normalised against the value obtained at 25 °C for each dispersion (the lowest value in both cases). The error of the measurement of STD factors is ca. 10%, in line with the previous reports [21].

increased significantly with temperature up to 80 °C, in CCNF dispersions it showed only a small enhancement up to 60 °C and a slight decrease at 80 °C (Fig. 5). The latter is probably due to the lower efficiency of intramolecular ^{1}H–^{1}H spin diffusion (cellulose saturation intrinsically lower) and intermolecular nuclear Overhauser effect (cellulose – HDO) at high temperature. It should be noted the hysteretic evolution of the STD factor of HDO in OCNF dispersions during the heat-cooling cycle (Fig. 5), is thus in agreement with the observed temperature-dependent rheological behaviour (Fig. 1). Notably, the increase in the STD factor of water in OCNF gels upon heating was found to be significantly higher at a lower concentration of OCNF (Fig. 5, †ESI, Fig. S8), in very good agreement with rheology where the highest concentration tested (4 wt%) showed only a small increase in G′ after the heating protocol (†ESI, Fig. S3d). Thus, the STD NMR experiments are directly reporting an increase in the fraction of OCNF-confined water molecules in the dispersion upon heating, which is not observed in the case of the CCNF dispersion. The increased fraction of OCNF-confined water observed upon heat-induced gelation is not due to conformational changes at the surface of OCNF fibrils (e.g. changes in the glycosidic bond torsion angles, or reorientation of the hydroxymethyl group in non-oxidised residues), but to changes at the mesoscale level, i.e. higher fibril-fibril overlap, in excellent agreement with the rheological and SAXS data.

In this way, we have demonstrated that STD NMR with observation of the residually protonated water molecules (HDO) is a simple powerful tool to study the hydration features of gels constituted by high molecular weight gelators (cellulose), reporting on changes in water confinement during gelation, and demonstrated the excellent correlation of the STD factor of the HDO peak to the rheological data of hydrogels prepared in D_2O.

3.4. Proposed mechanism of heat induced gelation of OCNF dispersions

The gelation of OCNF with increased temperature is the result of a delicate interplay of electrostatic and hydrophobic interactions in this system. As water is heated, the dielectric constant decreases, from 78.57 at 25 °C to 62.33 at 80 °C [51]. Decreased dielectric constant indicates a decreased polarizability of the fluid, which effectively acts as increased charge screening for electrostatic interactions. From our work on OCNF with added monovalent salt, increased charge screening causes the local aggregation of the fibrils, resulting in gelation [31] – only a small amount of added electrolyte is required to cross from repulsive interactions to attractive ones, as measured by SAXS [31]. Similarly, here heating causes some degree of flocculation in the OCNF suspensions, reducing light transmission, and a weak gel forms. This corresponds to the SAXS data which show no change in fibril cross section, but a change in the interaction parameter ν_{RPA} which indicates an increase in attractive interactions between the fibrils at higher temperatures. Gel formation is associated with an increase in confined water, seen by the STD NMR, since increased contact between fibrils will constrain water at the interfaces between the two surfaces (schematically depicted in Fig. 6). Once formed, after cooling the gel is in a metastable state, which is easily disrupted and returned to the dispersed state by agitation-induced shear. Increased charge screening would not alter the apparent hydrophobicity of the fibrils, so this is consistent with the fluores-

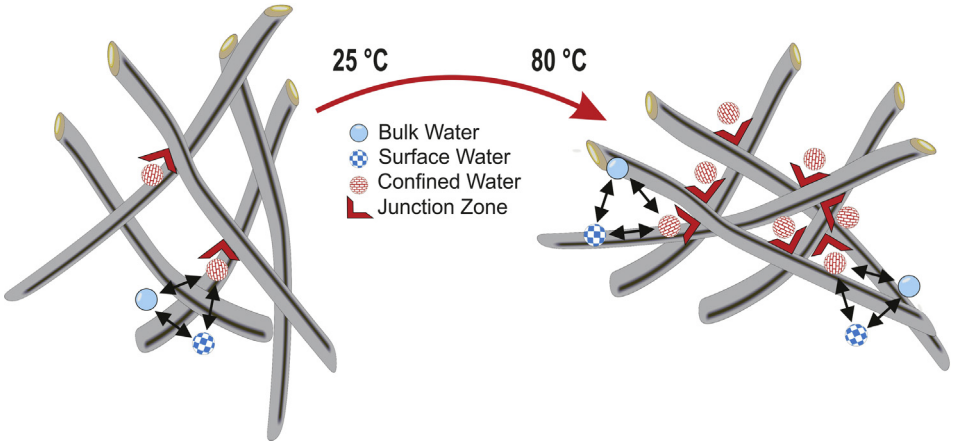

Fig. 6. Schematic representation of the increased overlap of the oxidised cellulose nanofibrils (OCNF) upon heating. After heating, the number of junction zones (highlighted in red) between fibrils increase, increasing the amount of confined water, without strong densification of the cluster. Note: cellulose fibrils and water molecules are not to scale.

cence data (†ESI, Fig. S6). CCNF is less responsive to electrostatic screening effects [52] due to the presence of stronger interfibrillar interactions as shown by SAXS (Fig. 4b) and by greater moduli (G′ and G″) in oscillatory rheology (Fig. 1b), hindering further fibrillar rearrangement upon heating. Since this suspension is already gelled, changes in dielectric constant and electrostatic screening make little difference to the structure.

4. Conclusion

In this work we describe a novel mechanism of temperature triggered gelation for oxidised nanocellulose hydrogels, along with a thorough study of the process, from the rheological macroscopic behaviour, through nanoscale fibril aggregation, down to the molecular level of the water dynamics within the OCNF network. Rheological measurements revealed that the negatively-charged OCNF forms a metastable physical gel upon heating. The OCNF heat-induced gels were preserved upon cooling, but easily disrupted by mechanical perturbation. However, same behaviour was not observed for the positively-charged CCNF at the same concentrations. This shows the gelation is specific to OCNF and not a general behaviour of nanocelluloses. SAXS analysis of the OCNF gels pointed towards an increase in junction zones between fibrils, indicating a transition from widely dispersed fibrils to closer contact. These junction zones work as crosslinking points creating a connected network that leads to the remarkable increase in the elastic moduli observed. STD NMR experiments detected an increase in the population of confined water with temperature, this behaviour not observed for CCNF, suggesting a correlation between water confinement and gel formation. We proposed that this heat-induced fibril aggregation is mainly driven by changes of the dielectric constant of the dispersing media (water) which alters the fine balance between attractive forces (interfibrillar hydrogen bonding and hydrophobic interactions) and repulsive forces (electrostatic interactions) favouring a closer interaction between the fibrils leading to the formation of a metastable aggregate and gel formation. For the CCNF, the attractive element of this balance is already stronger than for OCNF and the CCNF fibrils are already in a higher level of aggregation, as seen by SAXS, such that heating cannot meaningfully affect the gel structure further. These observations of gelation in OCNF due to heating are significant for proposed applications of these materials in rheology modification, since formulation and industrial processing frequently involve heating steps, which may therefore alter the properties of the suspension. The results outlined here will permit selection of nanocellulose properties and post-processing of suspensions to enhance or avoid this effect and inform further work towards uptake of such materials in real-life applications.

These results also demonstrate the strength of using combined non-invasive, *in situ* techniques to probe the gel properties from nanoscale using SAXS to molecular scale using STD NMR, giving detailed insights into mechanism. In particular the work shows the benefits of using STD NMR on residual HDO in D_2O solvated hydrogel samples of particulate gelators to monitor changes in the populations of surface-confined water molecules with temperature. The ease of the STD NMR methodology, and the solid evidence gathered in this work may allow a future boost in the use of HDO-based STD NMR experiments to correlate changes in confined water populations with rheology, within the hydrogel research community.

Acknowledgements

V.C. thanks University of Bath for supporting his PhD. J.C.M.G. thanks EPRSC for funding (EP/N033337/1). M.A.D.S. and J.S. thank EPRSC for funding this project (grant EP/N033310/1). The authors would like to thank Valeria Gabrielli for helping with the acquisition of NMR experiments, as well as the Diamond Light Source for the award of beam time (experiment no. SM16364), and Drs Nick Terrill, Andy Smith, and Tim Snow for their assistance with the experiments on beamline I22. We also acknowledge access to UEA Faculty of Science Research Facilities. Additional research data supporting this publication are available as electronic supplementary files at DOI: 10.15125/BATH-00476 and https://people.uea.ac.uk/en/datasets/data-for-understanding-heat-driven-gelation-of-anionic-cellulose-nanofibrils-combining-saturation-transfer-difference-std-nmr-small-angle-xray-scattering-saxs-and-rheology(a524288d-b4ac-4b6e-a40a-3a6dd1677d3c).html.

Conflict of interest

The authors declare no conflicts of interest.

Appendix A. Supplementary material

Supplementary data to this article can be found online at https://doi.org/10.1016/j.jcis.2018.09.085.

References

[1] T. Saito, S. Kimura, Y. Nishiyama, A. Isogai, Biomacromolecules 8 (2007) 2485–2491.
[2] A. Isogai, T. Saito, H. Fukuzumi, Nanoscale 3 (2011) 71–85.
[3] D. Celebi, R.H. Guy, K.J. Edler, J.L. Scott, Int. J. Pharm. 514 (2016) 238–243.
[4] J. Coombs O'Brien, L. Torrente-Murciano, D. Mattia, J.L. Scott, ACS Sustain. Chem. Eng. 5 (2017) 5931–5939.
[5] L. Li, Macromolecules 35 (2002) 5990–5998.
[6] R.J. Crawford, K.J. Edler, S. Lindhoud, J.L. Scott, G. Unali, Green Chem. 14 (2012) 300–303.
[7] K.J. De France, T. Hoare, E.D. Cranston, Chem. Mater. 29 (2017) 4609–4631.
[8] T. Saito, T. Uematsu, S. Kimura, T. Enomae, A. Isogai, Soft Matter 7 (2011) 8804–8809.
[9] D. da Silva Perez, S. Montanari, M.R. Vignon, Biomacromolecules 4 (2003) 1417–1425.
[10] Y. Okita, T. Saito, A. Isogai, Biomacromolecules 11 (2010) 1696–1700.
[11] S. Tsuguyuki, A. Isogai, Biomacromolecules 5 (2004) 1983–1989.
[12] H. Fukuzumi, R. Tanaka, T. Saito, A. Isogai, Cellulose 21 (2014) 1553–1559.
[13] Y. Habibi, H. Chanzy, M.R. Vignon, Cellulose 13 (2006) 679–687.
[14] N. Quennouz, S.M. Hashmi, H.S. Choi, J.W. Kim, C.O. Osuji, Soft Matter 12 (2015) 157–164.
[15] H. Dong, J.F. Snyder, K.S. Williams, J.W. Andzelm, Biomacromolecules 14 (2013) 3338–3345.
[16] N. Masruchin, B.D. Park, V. Causin, I.C. Um, Cellulose 22 (2015) 1993–2010.
[17] M. Hasani, E.D. Cranston, G. Westman, D.G. Gray, Soft Matter 4 (2008) 2238–2244.
[18] M. Zaman, H. Xiao, F. Chibante, Y. Ni, Carbohydr. Polym. 89 (2012) 163–170.
[19] Y.E. Shapiro, Prog. Polym. Sci. 36 (2011) 1184–1253.
[20] C.L. Cooper, T. Cosgrove, J.S. van Duijneveldt, M. Murray, S.W. Prescott, Soft Matter 9 (2013) 7211.
[21] S.M. Ramalhete, K.P. Nartowski, N. Sarathchandra, J.S. Foster, A.N. Round, J. Angulo, G.O. Lloyd, Y.Z. Khimyak, Chem. – A Eur. J. 23 (2017) 8014–8024.
[22] K. Zhang, S. Fischer, A. Geissler, E. Brendler, Carbohydr. Polym. 87 (2012) 894–900.
[23] J.C. Courtenay, M.A. Johns, F. Galembeck, C. Deneke, E.M. Lanzoni, C.A. Costa, J. L. Scott, R.I. Sharma, Cellulose 24 (2016) 253–267.
[24] V. Calabrese, M.A. da Silva, J. Schmitt, J.C. Muñoz-Garcia, V. Gabrielli, J.L. Scott, J. Angulo, Y.Z. Khimyak, K.J. Edler, Soft Matter (2018), https://doi.org/10.1039/c8sm00752g.
[25] I.T. Norton, F. Spyropoulos, P. Cox, Chemical Engineering, Wiley-Blackwell, 2011, pp. 10–15.
[26] C.A. Haskard, E.C.Y. Li-Chan, J. Agric. Food Chem. 46 (1998) 2671–2677.
[27] J.S. Pedersen, Adv. Colloid Interface Sci. 70 (1997) 171–210.
[28] J.C. Courtenay, S.M. Ramalhete, W.J. Skuze, R. Soni, Y.Z. Khimyak, K.J. Edler, J.L. Scott, Soft Matter 14 (2018) 255–263.
[29] S. Manet, J. Schmitt, M. Impéror-Clerc, V. Zholobenko, D. Durand, C.L.P. Oliveira, J.S. Pedersen, C. Gervais, N. Baccile, F. Babonneau, I. Grillo, F. Meneau, C. Rochas, J. Phys. Chem. B 115 (2011) 11330–11344.
[30] T. Shimada, M. Doi, K. Okano, J. Chem. Phys. 88 (1988) 2815–2821.
[31] J. Schmitt, V. Calabrese, M.A. Silva, S. Lindhoud, V. Alfredsson, J.L. Scott, K.J. Edler, Phys. Chem. Chem. Phys. 20 (2018) 16012–16020.
[32] M. Mayer, B. Meyer, J. Am. Chem. Soc. 123 (2001) 6108–6117.
[33] C.A. Lepre, J.M. Moore, J.W. Peng, Chem. Rev. 104 (2004) 3641–3676.
[34] S.J. Veen, P. Versluis, A. Kuijk, K.P. Velikov, Soft Matter 11 (2015) 8907–8912.

[35] J. Araki, M. Wada, S. Kuga, T. Okano, Colloids Surfaces A Physicochem. Eng. Asp. 142 (1998) 75–82.
[36] A.J.M. Nic, J. Jirat, B. Kosata, IUPAC. Compendium of Chemical Terminology, 2nd ed. (the 'Gold Book'), Compiled by A. D. McNaught and A. Wilkinson. Blackwell Scientific Publications, Oxford, 1997.
[37] D. De Kort, S. Veen, H. Van As, D. Bonn, K. Velikov, J. Van Duynhoven, Soft Matter 12 (2016) 4739–4744.
[38] B. Hammouda, in: Probing Nanoscale Structures - The SANS toolbox, National Institute of Standards and Technology Center for Neutron Research Gaithersburg, 2010, pp. 211–225.
[39] Y. Su, C. Burger, B.S. Hsiao, B. Chu, J. Appl. Crystallogr. 47 (2014) 788–798.
[40] Y. Mao, K. Liu, C. Zhan, L. Geng, B. Chu, B.S. Hsiao, J. Phys. Chem. B 121 (2017) 1340–1351.
[41] F. Cherhal, F. Cousin, I. Capron, Langmuir 31 (2015) 5596–5602.
[42] G. Beaucage, J. Appl. Crystallogr. 28 (1995) 717–728.
[43] L. Wu, C.P. Ortiz, D.J. Jerolmack, Langmuir 33 (2017) 622–629.
[44] S. Lazzari, L. Nicoud, B. Jaquet, M. Lattuada, M. Morbidelli, Adv. Colloid Interface Sci. 235 (2016) 1–13.
[45] Y. E. Shapiro, ed. P. Somasundaran, CRC Press, New York, USA, Encycloped., 2006, p. 1219.
[46] C. Mayer, Prog. Nucl. Magn. Reson. Spectrosc. 40 (2002) 307–366.
[47] F. Jiang, J.L. Dallas, B.K. Ahn, Y. Lo Hsieh, Carbohydr. Polym. 110 (2014) 360–366.
[48] H. O'Neill, S.V. Pingali, L. Petridis, J. He, E. Mamontov, L. Hong, V. Urban, B. Evans, P. Langan, J.C. Smith, B.H. Davison, Sci. Rep. 7 (2017) 1–13.
[49] M. Mayer, B. Meyer, Angew. Chemie - Int. Ed. 38 (1999) 1784–1788.
[50] M.D. Segarra-Maset, B. Escuder, J.F. Miravet, Chem. - A Eur. J. 21 (2015) 13925–13929.
[51] G.P. Srivastava, Y.P. Varshni, Physica 22 (1956) 584–586.
[52] J.C. Courtenay, Y. Jin, J. Schmitt, K.J. Edler, J.L. Scott, 2018 (in preparation).